University of Memphis

University of Memphis Digital Commons

Electronic Theses and Dissertations

7-28-2020

Calculations of Vacancy Diffusivity in WO3

Juan Chen

Follow this and additional works at: https://digitalcommons.memphis.edu/etd

Recommended Citation

Chen, Juan, "Calculations of Vacancy Diffusivity in WO3" (2020). *Electronic Theses and Dissertations*. 2105.

https://digitalcommons.memphis.edu/etd/2105

This Thesis is brought to you for free and open access by University of Memphis Digital Commons. It has been accepted for inclusion in Electronic Theses and Dissertations by an authorized administrator of University of Memphis Digital Commons. For more information, please contact khggerty@memphis.edu.

CALCULATIONS OF VACANCY DIFFUSIVITY IN WO_3

By

Juan Chen

A Thesis

Submitted in Partial Fulfillment of the

Requirements for the Degree of

Master of Science

Major: Physics and Materials Science

The University of Memphis

August 2020

Copyright© Juan Chen

All rights reserved

Dedicated to my dad: may you always be proud of me

Acknowledgments

First, I want to thank my advisor, Doctor Xiao Shen, for directing and supporting my research. I learned much about solid-state physics under Doctor Shen’s tutelage. His continued patience and willingness to help were crucial for the completion of my research.

Secondly, I want to thank my partner, Romakanta Bhattarai. As a senior Ph.D. student in our group, he taught me how to use the VASP software. His experience with VASP helped prevent many mistakes and made work more efficient.

I also want to thank my parents for supporting me throughout my education, financially and mentally. Their trust gives me confidence and pushes me forward.

Finally, I am thankful for my classmates and friends who have accompanied me throughout these two years. We have overcome many challenges, and they always encouraged me. I wish them the best in their studies.

The University of Memphis

Abstract

College of Arts and Sciences

Department of Physics and Materials Science

Master of Science

Calculations of Vacancy Diffusivity in WO_3

by Juan Chen

The memristor is viewed as a promising material to store digital information and has analog applications that drew researchers' attention. Researchers explored the possibilities of using memristors to simulate synapses in the human brain. WO_3 is one of the materials that can make memristors. Based on the mechanism of memristors, we know the motion of defects in WO_3 changes the Schottky barrier and the current; thus, it can make the switch between high resistance state, HRS, and low resistance state, LRS. This paper will explore vacancy diffusivity in WO_3. In this research, we concentrate on the cubic and monoclinic structure of WO_3. We use the first principle density functional theory or DFT, and hybrid DFT to calculate the formation energy of different charge states of oxygen vacancies in WO_3 and plot the graph of Fermi level to find the charge state with the lowest formation energy conditions. We use the nudged elastic band method to get the energy barrier for the vacancies to travel inside the structure.

Contents

Introduction **1**

Literature Review **3**

2.1 Characteristic of memristor 3

2.2 Mechanism 4

2.2.1 Filamentary switching 4

2.2.2 Interfacial switching 5

2.3 Application 7

2.3.1 Memory application 7

2.3.2 Analog application 8

2.4 WO_X 10

2.5 Status and prospects 11

Method **12**

3.1 Determine the most stable charge state from DFT results 12

3.2 Nudged elastic band method (NEB) 13

3.3 Density Functional Theory (DFT) and Hybrid DFT 14

3.4 Problem setup 16

Results and Discussion **18**

4.1 Cubic phase 18

4.2 Monoclinic phase.. 20

4.2.1 One vacancy.. 22

4.2.2 Two vacancies.. 25

Conclusions and Future Work 29

Reference 30

Chapter 1

Introduction

As computers have become more prominent in our daily life, human demand for computers has become higher and higher. All computers use the Von Neumann structure [1], the arithmetic unit and the storage unit are separate, resulting in the transfer of a large amount of information between the processor and the memory which consumes a lot of energy. In contrast, the human brain has the advantages of parallel computing and relatively low energy consumption. Therefore, researchers have explored a new type of computing method, brain-like computing [2]. It aims to achieve low-power computing power the brain by simulating the interaction between neurons [3]. In the beginning, the traditional silicon-based complementary metal-oxide semiconductor, or CMOS [4], was popularly used to process devices. However, the current random neurons with excitation and suppression connections based on traditional CMOS require at least twice the extremely high hardware overhead of the excitation neurons, which is not conducive to high-density, large-scale impulsive neural network integration. Researchers turned their attention to a kind of new material—memristor.

The memristor concept was proposed by Leon Chua in 1971[5], [6], [7]. Resistance (R), capacitor (C), and inductor (L) already connected four basic physics variables, including voltage (v), current (i), charge (q), and magnetic flux (φ) [8], but the relationship network is not complete. Leon Chua proposed that there should be a circuit element memristance (M) in nature, which represents the relationship between magnetic flux (φ) and electric charge (q) (Figure 1.1).

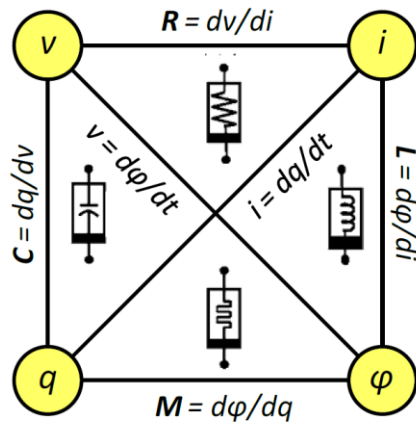

Figure 1.1 Relationship between four basic components of a circuit.[9]

Memristor is the combination of the word memory and resistor [6], [9]. Memristors can generate and maintain a safe current through a device just like resistors. The difference between memristor and resistor is that memristors can memorize the amount of charge that goes through it even after the power is turned off [10]. Many memristors have a metal/insulator/metal (MIM) sandwich structure [11]. The insulator is usually a metal oxide such as NiO, Cu_2O [12], TiO_2 [13], WO_3 [14], ZnO [15], [16], which has a high concentration of vacancies.

Chapter 2

Literature Review

2.1 Characteristic of memristor

Memristors exhibit non-linear conductive behavior [17] which is due to the coupled electronic and ionic conduction mediated by defects. It can switch between high resistance state, or HRS, and low resistance state, or LRS [18], [19]. Memristors are materials that have a nonlinear characteristic in their I-V curves. Some memristors [20] have an abrupt change in their I-V curves (like Figure 2.1 (a)), while other memristors' [21] I-V curves look like figure "8" (like Figure 2.1(b)).

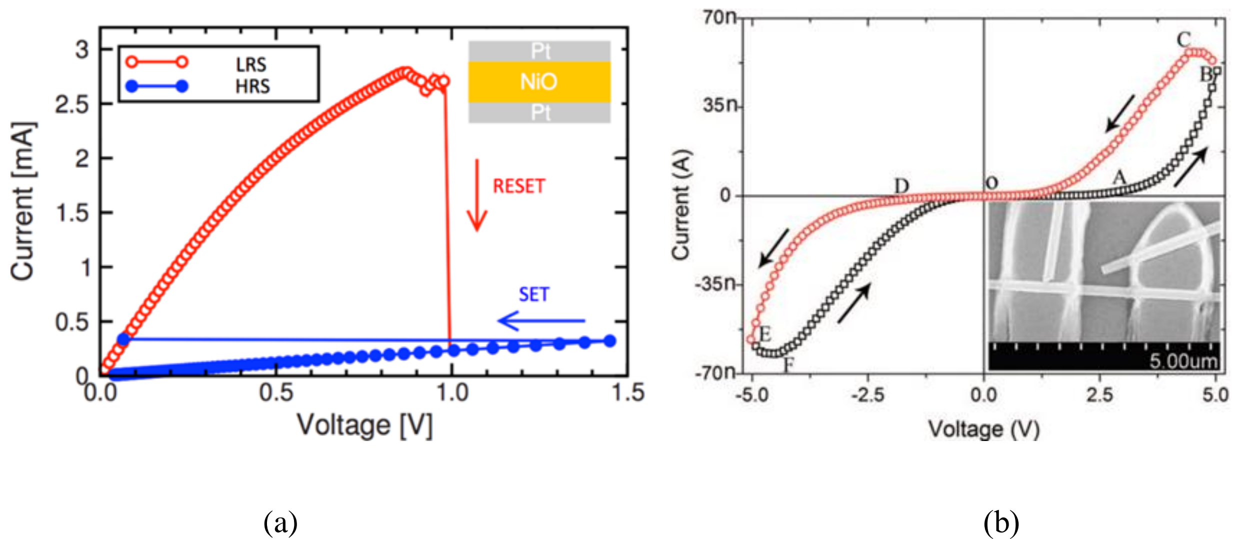

Figure 2.1 The I-V curve of memristors. (a) Switching in a Pt/NiO/Pt sandwich structure in the condition of HRS and LRS [22]. (b) Switching in a Pd/WOx/W sandwich structure. The arrows show a directional sweep [23].

Figure 2.1 (a) shows that after an application of an external voltage on the sandwich structure, the resistance keeps increasing, noted by the HRS trend. When the external voltage

reaches a certain value, it triggers the set process. The resistance changes from 100 kΩ to 200 Ω [16]. As the voltage increases, the resistance increases as well, shown in the LRS trend. The reset process will be suddenly triggered when the current reaches the threshold level, noted by an abrupt change in resistance. In Figure 2.1 (b), the resistance of WO_3 gradually changes until it reaches the threshold and switches from a high resistance state (the black trendline in the graph) to a low resistance state (the red trendline). The graph is a loop. These two memristors have very different I-V curves because they have different mechanisms in their systems which we will discuss later.

2.2 Mechanism

The I-V curve of memristors can exhibit two types of switching behavior: one is an abrupt change in resistance (such as NiO), the other one is gradual change (such as WO_3). Thus, there are two kinds of mechanisms in memristor: filamentary switching and interface-type switching.

2.2.1 Filamentary switching

Some memristors have filamentary switching mechanism [24], [12]. It starts with a metal oxide that has a high concentration of oxygen vacancies between two electrodes [25], and the resistance is high. As the oxygen vacancies accumulate, there is a filament that starts to form which connects the positive and negative terminal of the electrodes, shown in Figure 2.2 (a). At this point, resistance changes from HRS to LRS. Since the continuous high current generates heat, the vacancies start to migrate and cause the rupture of the filament and connection, shown in Figure 2.2 (b). Thus, the condition switches back from LRS to HRS after cycling.

a.

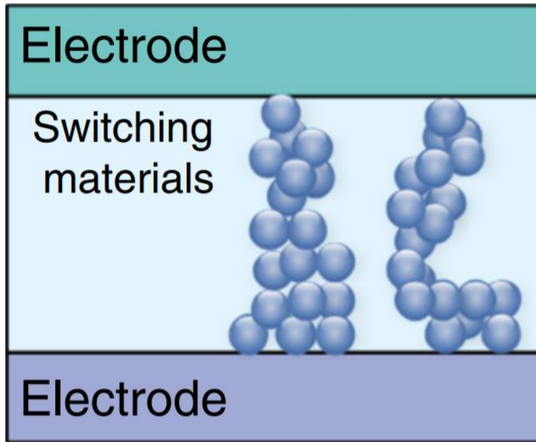

b.

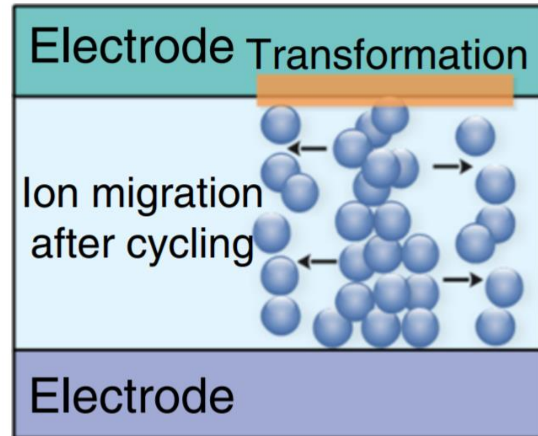

Figure 2.2 Filamentary conducting path. (a) formation of filament [26]. (b) filament ruptured after cycling [26].

2.2.2 Interfacial switching

Some memristors have interfacial switching mechanism [27]. There are two types of contact between semiconductor and metal: Schottky contact [28] and ohmic contact [29]. Just like the PN junction, Schottky contact has the rectification characteristics which are decided by the bandgap, doping type, and concentration of the semiconductor and the work function of the metal [30]. When metals have contact with n-type semiconductors, the band of the semiconductor near the interface has a bending, leading to the Schottky barrier.

Figure 2.3 is an illustration of the Schottky barrier. ϕ_m is the work function which is the minimum energy needed for electrons to escape into the vacuum level. χ is the electron affinity, which is the energy released when electrons drop from the vacuum level to the bottom of the conduction band. The ϕ_B is the height of the Schottky barrier and $\phi_B = \phi_m - \chi$. The E_C is the conduction band minimum energy; E_V is the valance band maximum energy, and E_F is the Fermi level. We do not want the Schottky barrier to exist in most situations. There are two ways to

reduce the Schottky barrier. One is to lower the height of the barrier ϕ_B, so the electrons do not need such high energy to jump the barrier. The other one is to narrow the width of the barrier, making the electrons tunnel through it easier. WO_3 uses the second way to reduce the Schottky barrier (Figure 2.4).

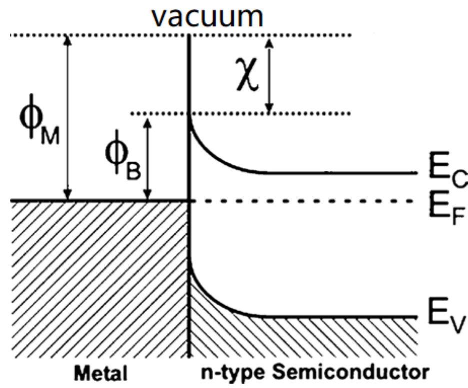

Figure 2.3 Illustration of Schottky barrier [31]

In Figure 2.4 (a), Schottky barrier width W_D is big in metal-WO_3-metal cases. In Figure 2.4 (b), the accumulation of vacancies narrows the Schottky barrier width and allows electrons tunnel through it, resulting in alters of current. That is the reason why resistance can change from HRS to LRS. Therefore, we need to understand the motion of the defects in WO_3.

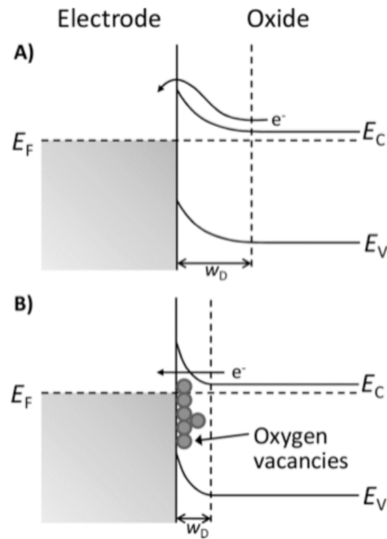

Figure 2.4 The interface mechanism for switching in WO_3 [32]. (A) The band diagram for HRS. (B) The band diagram for LRS.

2.3 Application

After discussing the mechanism of the memristors, we would like to talk about the application of memristors.

2.3.1 Memory application

Nowadays, there are two types of random-access memory, RAM: volatile and non-volatile [33]. The volatile memory includes dynamic random-access memory, DRAM, and static random-access memory, SRAM [34]. DRAM loses data when the power is suddenly turned off and SRAM is physically bulky which would require a lot of space to create a large capacity memory storage. Therefore, neither are ideal memory types to store information.

The classical example of non-volatile memory is flash memory [35]. It is made of metal-oxide-semiconductor and filed-effect-transistor [36]. The flash memory has some disadvantages, including low operation speed [37], limited write/erase cycles [38], and high voltage requirement [39]. A lot of research has been done on applying memristors in the memory storage field.

HP company creates TiO_2 memristor [40] devices which can be explained by Chua's model in 2008, hence proved the existence of memristors. It was a milestone on the way of developing a new type of computer memory.

2.3.2 Analog application

Another application of memristor is in the analog field. Researchers are working on using memristors to mimic the behaviors of synapses, such as parallel computing. A synapse is a place where two neurons contact each other and transmit information [41]. For most neurons in the central nervous system, synapses are the only input channels for their neural signals. The neurons in the central nervous system are interconnected in the form of synapses [42], which in turn form a complex network of neurons.

Synaptic plasticity [43] is a characteristic or phenomenon in which the shape, function, strength, and efficiency of synapses undergo a series of permanent changes. The reason we can use memristors to simulate synapses is that memristors have the same kind of plasticity. Besides, its specifications are nanoscale, which makes it possible to use it to build a brain-like computing device in the future. Figure 2.5 illustrates the analogy between a memristor and a synapse. The electrodes in the memristor can be viewed as a neuron pair, and the semiconductor in the middle works as a synapse. Oxygen vacancies or charge carrier transition resembles neurotransmitters going through the synapse.

a.

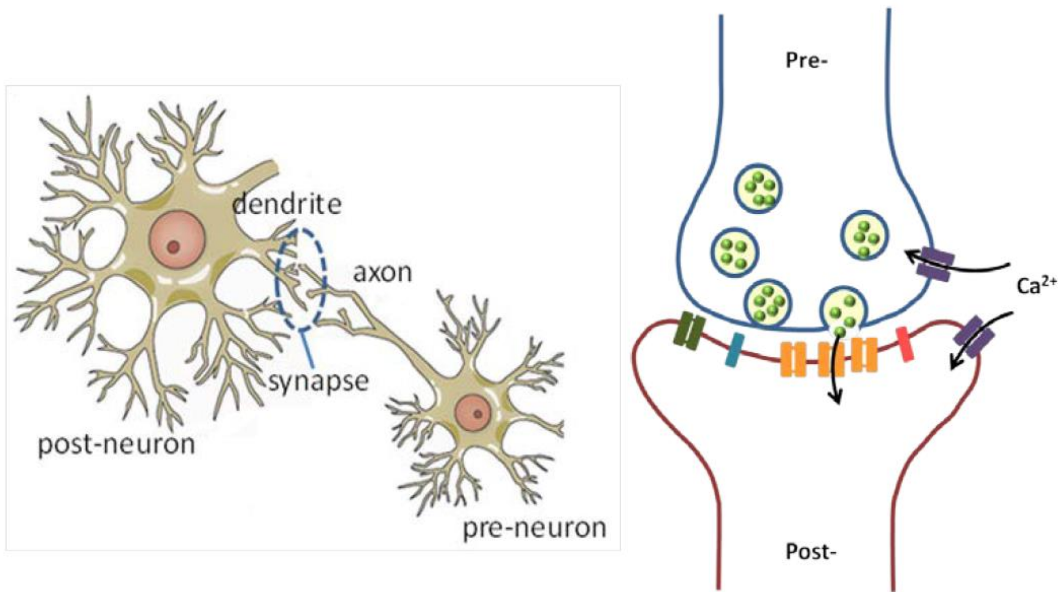

b.

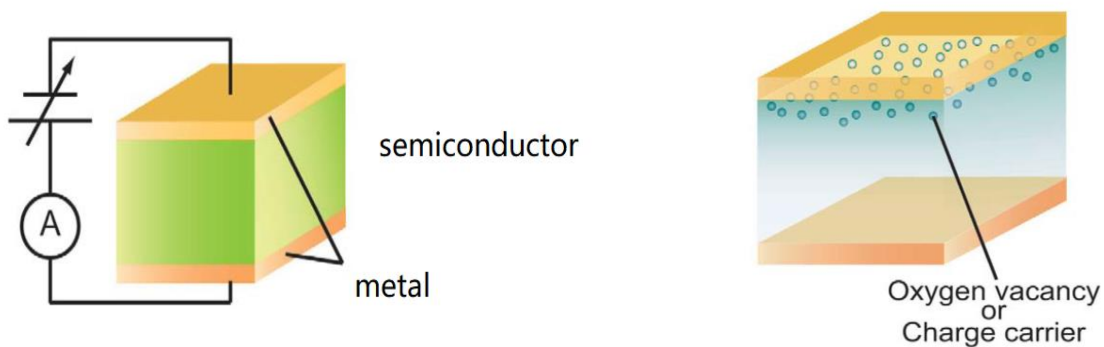

Figure 2.5 (a) Illustrations of a synapse (left) and neurotransmitters transition (right) [44]. (b) Sketch of MIM sandwich structure (left) and atomic version of vacancy transition [12].

"Synaptic weight" determines the number and size of neurotransmitter vesicles released by nerve stimulation signals during signal transmission between neurons [45]. It is sometimes interpreted as the strength of the connection between synapses. The conductive state of the

memristor represents the change of the synaptic weight [46] (the increase/ decrease of conductivity correspond to the increase/ decrease of the synaptic weight, respectively). By changing the pulse voltage shape [47], frequency [48], duration [49], and other parameters we can simulate characteristics of different nerve stimulation signals, and obtain the corresponding change of the conductive state. The change of the conductive state is electrostatic [50]. In 2019, Dr. Lu's group made 6 hybrid neuromorphic memristor chips (Figure 2.6).

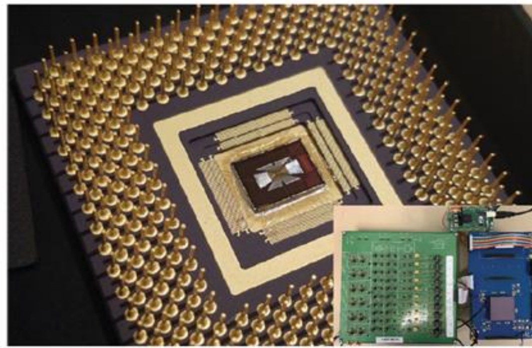

Figure 2.6 Hybrid neuromorphic memristor chip made by Dr. Lu's group at the University of Michigan [51].

2.4 WO_X

Metal-WO_X-Metal sandwich structure can be used to mimic synapse behavior. WO_X is WO_3 with vacancies inside it. The concentration of oxygen depends on the value of $_X$, and the structure of WO_3 depends on temperature. It can be cubic, monoclinic, triclinic, orthorhombic, or tetragonal under different temperatures. Monoclinic is the most common one.

WO_X is an n-type semiconductor and its electrical resistivity depends on x. WO_3 is an insulator. When there are oxygen vacancies in the WO_3 structure, the deficiency of oxygen will

make WO_X become a semiconductor. For WO_X memristor, electrodes of the MIM sandwich structure usually can be Pd, Pt, or Au [52].

The interaction between oxygen vacancies inside WO_3 will affect the diffusivity. To accurately model switching behavior, we need to determine the motion of vacancies. We need to understand the process of induvial oxygen vacancy diffusion, then observe what will happen if they react with each other.

2.5 Status and prospects

Nowadays, there are some engineering models of memristors. But they are all phenomenological models. They can only be used for fitting data, not for further understanding of memristors. A physical model not only can help us understand the plasticity (adjustable properties of synaptic connection strength) in memristive synapses but also is useful for designing and operating memristive synapses. That is the reason we do this research.

Since we want to know the diffusivity of vacancies in WO_X and the diffusivity depends on the charge state of the vacancy, we need to obtain the most stable charge state first. Plotting the defect formation energy graph will be helpful. Meanwhile, the nudged elastic band (NEB) method can find the minimum energy path for vacancies migrating from one position to another. Since the total energies are involved in NEB and defect formation energy, we need to use density functional theory (DFT) or hybrid DFT to calculate them. All the methods we used here will be discussed in the next chapter.

Chapter 3

Method

3.1 Determine the most stable charge state from DFT results

In our flow chart of research, the first step is using the defect formation energy graph to obtain the most stable charge state for WO_X. Here, we start from formation energy first.

The flowing formula shows how to get formation energy.

$$E^{f}_{(xq)} = E_{total}[x^q] - E_{total}[bulk] - \Sigma n_i \mu_i + qE_F + E_{rror} \quad (1)$$

$E_{total}[x^q]$ is the total energy of the supercell which has vacancies, $E_{total}[bulk]$ is the total energy of the non-defect supercell. These two total energies need to use DFT or hybrid DFT to calculate. $\Sigma n_i \mu_i$: n_i is the change of the number of the atoms, if there is one vacancy, the value will be −1; if one atom is added in, the value will be +1. μ_i is the chemical potential, q is the charge state, and E_F is the sum of valence band maximum and change in chemical potential. The correction value E_{rror} depends on the charge state.

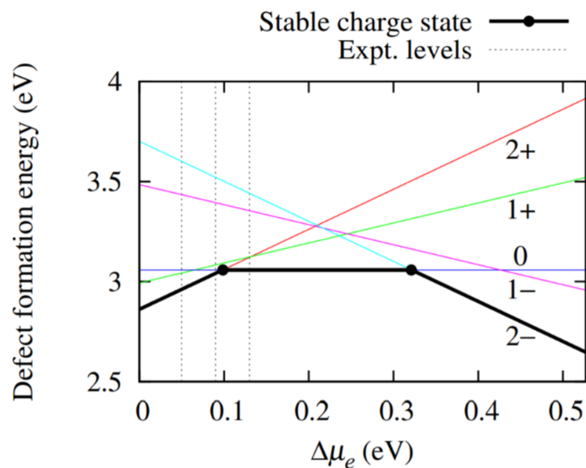

Figure 3.1 Formation energy of different charge states in Silicon [53].

Once we finish calculating the formation energy of each charge state, we can plot the Fermi level graph. For Figure 3.1 the left side of the graph should be the valence band maximum and the right side is the conduction band minimum. The x-axis is the change in the chemical potential. For the same $\Delta\mu_e$, if the formation energy is lower, it consumes less energy to form the vacancy, so that charge state will be the most stable charge state at that time. For example, for $\Delta\mu_e$ from 0 to 0.09 eV, the 2+ charge state will be the most stable one.

3.2 Nudged elastic band method (NEB)

After we achieve the most stable charge state, we can work on the diffusion of vacancies in these charge states conditions. Using the nudged elastic band method is a good way to find the minimum energy consumption path for the vacancies' diffusion. Figure 3.2 illustrates the process of the NEB method. For example, we have the initial position A and final position B, and we want to know the path between A and B. Firstly, we need to use the density of functional theory to get the minimum energy of initial state and final state, which will be discussed later.

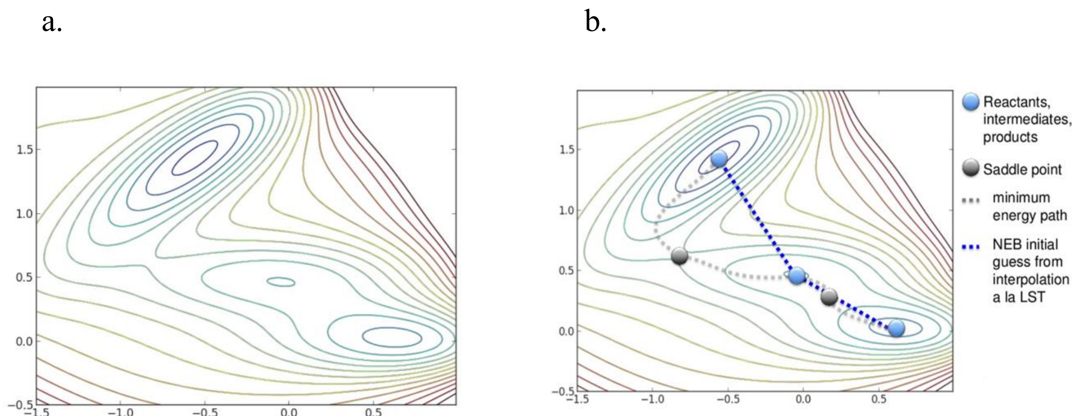

Figure 3.2 Illustration of NEB method process

Set several imaginary images between the initial and final states, and all these states are constrained by the spring interactions like small balls connected with a rubber band. The force each of them gets is

$$\vec{F_i} = -\vec{\nabla} V\left(\vec{R_i}\right) + K\left(R_{i+1} - R_i\right) - K\left(R_i - R_{i-1}\right) \quad (2)$$

The nudged elastic band method makes these "balls" that vibrate on the energy landscape adjust their positions. Finally, the force formula becomes easier.

$$F_i = F_i^s|_{||} - \nabla E(R_i)| \perp \quad (3)$$

The component of the spring force parallel to the path is completely retained, and the component of the force from potential perpendicular to the path will guide the structure to move correctly. This is how the NEB will help numerical converge. Here, we use density functional theory to obtain the value of the spring force parallel to the path.

3.3 Density Functional Theory (DFT) and Hybrid DFT

In quantum mechanics, the Schrödinger equation we usually see is a single electron equation. However, the materials we are interested in have a lot of electrons. The Schrödinger equation becomes a many-body equation that cannot be solved systematically due to the interaction between the electrons. Density functional theory is one of the solutions to this problem.

Before we move to DFT, we need to know Born Oppenheimer approximation [54]. The general idea is that the mass of the nuclei is much bigger than electrons; therefore, the dynamics of the nuclei and electrons can be decoupled. Then we can concentrate on solving the ground

state of electrons. The Hamiltonian can be the summation of kinetic energy, potential energy, and electron-electron Coulomb interaction. The formula can be written as:

$$\hat{H} = -\frac{\hbar^2}{2m_e}\sum_i^N \nabla_i^2 + \sum_i^N V_{ext}(r_i) + \sum_{i<j}^N U_{(r_i,r_j)} \quad (4)$$

DFT is based on the Hohenberg-Kohn theorem [55] and Kohn-Sham ansatz [56]. The Hohenberg-Kohn theorem was promoted in 1964, and it has two main ideas: The energy of the ground state in the Schrödinger equation is a function of electron density; the electron density with the lowest energy is the solution to the Schrodinger equation [57], [58]. Making the whole problem based on electron density causes the degree of freedom of the Schrödinger equation has dropped from 3N to 3.

In the Hohenberg-Kohn theorem, they promoted using electron density instead of wave function without providing the method to obtain ground state electron density [59]. One year later, Kohn and Sham solved this problem. They consider the whole system as a non-interaction system. At the same time, use the single electron wave function. The following eigenvalue equation is the famous Kohn-Sham equation.

$$\left(-\frac{\hbar^2}{2m}\nabla^2 + v_{eff(r)}\right)\varphi_{i(r)} = \varepsilon_i \varphi_i(r) \quad (5)$$

Then they had a self-consistency scheme: guess a density of electron ρ(r) first, then use it to solve the Kohn-Sham equation to get φi (r). Afterall, recalculate the electron density by using the following formula:

$$\rho(r) = \sum_i^N |\varphi_i(r)|^2 \quad (6)$$

If the ρ(r) we get from the calculation is the same as the one we guessed at the beginning, this is the perfect ground state electron density we want. Otherwise, start the guessing ρ(r)

->getting $\varphi_i(r)$ ->recalculating $\rho(r)$ loop again and again until getting the right answer. Hybrid DFT is the mixture of the standard DFT and the Hartree-Fock exchange [60].

3.4 Problem setup

After learning the basic knowledge of WO_3 and all the methods, let me sort out what we need to do. In our cases, we focus on the monoclinic and cubic structure of WO_3. To make the defect-to-defect interaction to be small enough that we can neglect it, we need to make a supercell of WO_3. Too many atoms in the structure make a complete DFT calculation, here we need to use the special k-point (1/4,1/4,1/4) to accelerate the calculation. We set cut-off energy at 400V.

The hybrid DFT can get a more accurate value of the total energy and bandgap. Therefore, we use this method to calculate the formation energy of one vacancy and two vacancies to get the most stable charge states for these two conditions.

For the one vacancy, we will consider the condition of 2+, 1+, 2-, 1- and neutral for the monoclinic structure. For the two vacancies, we will try 1+, 2+, 3+, 4+, 1-, 2-, 3-, 4- and neutral settings. After we achieve the most stable charge states, we will calculate the energy barrier of these charge states. Also, we need to research how two vacancies react with each other by calculating the diffusion energy barrier near another vacancy. For example, we have two vacancies here initially, they are on the position A1 and A2 (Figure 3.3). The vacancy on A2 position does not move, while the vacancy on A1 position migrates to C position. During the whole process, there is an interaction between these two vacancies; what we want to see is how the vacancy on A2 position affects the other vacancy's migration.

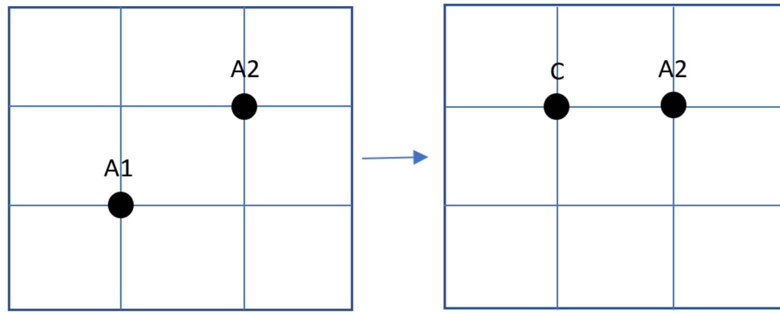

Figure 3.3 Illustration of two vacancies migration process. The black dots represent vacancies.

Chapter 4

Results and Discussion

4.1 Cubic phase

WO_3 can be cubic, monoclinic, triclinic, orthorhombic, or tetragonal phase under different temperatures. Here, we did calculations on the cubic and monoclinic phases.

The first part of this research is based on the cubic phase. Since oxygen vacancy is a shallow donor, in other words, it is most stable in the 2+ charge state (Vo^{2+}) [61] and does not introduce deep levels in the bandgap, we set two valence electrons less than it should be in this case.

The cubic bulk is shown in Figure 4.1 (a). After relaxing the bulk structure, the lattice parameter we get from the hybrid DFT calculation is 3.77 Å, which is the same as the experimental value. To reduce the interaction between periodic images of vacancy, we make a 108-atom supercell (Figure 4.1(b)). Firstly, we remove one oxygen atom from the supercell to make a vacancy defect (Figure 4.1(c)). Then, we relax the atomic coordinates by fixing lattice parameters to get the initial vacancy position state. Next, we look for the nearest oxygen atom and modify its coordinates to make it switch position with the vacancy (Figure 4.1(e)). Relax the structure to get the minimum final state energy as well. Finally, we use the NEB method to track the oxygen vacancy migration to the nearest spot and find the state of the highest energy in the whole process which is called transition state (Figure 4.1 (d)). The motion of a vacancy is the same as an atom moving in the opposite direction. For example, the vacancy migration from A to

B is equivalent to the migration from B to A. Therefore, we can track vacancies by tracking atoms that switch positions with those vacancies.

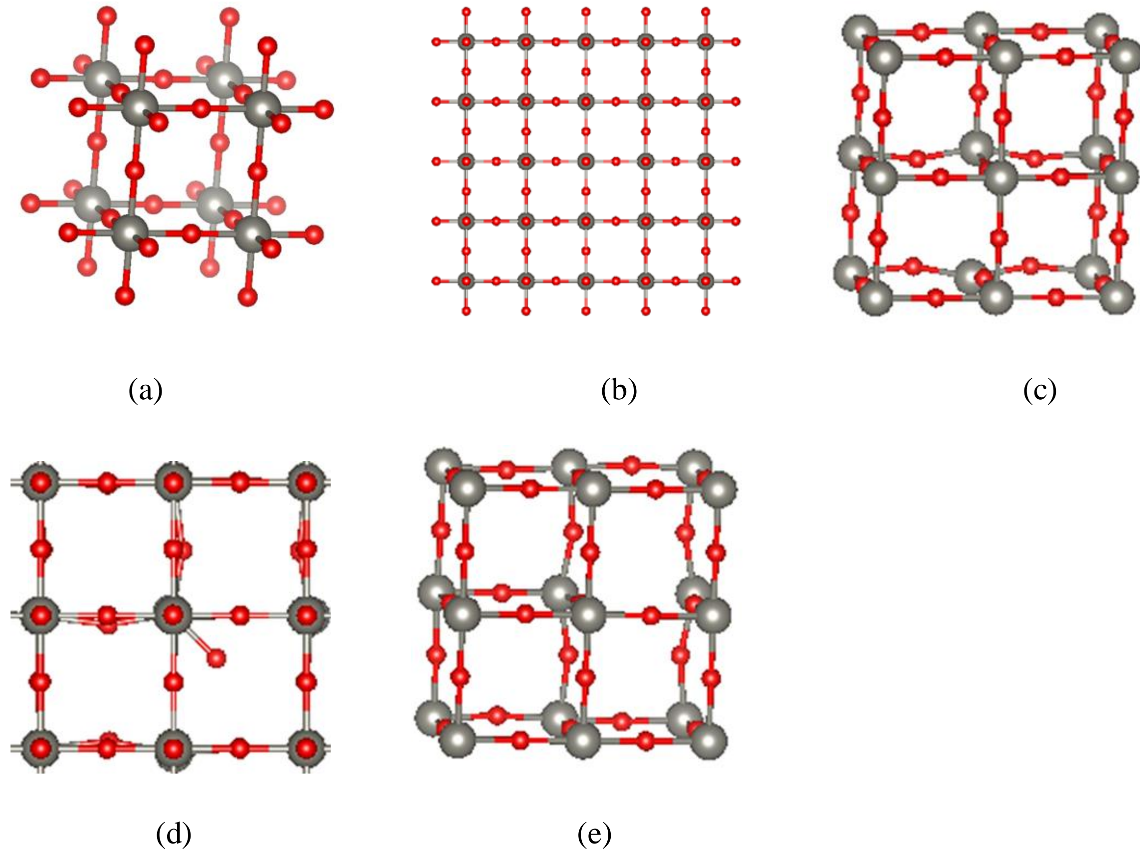

Figure 4.1 The migration of oxygen vacancy in WO_3. (a) cubic bulk of WO_3. (b)WO_3 supercell. (c) the initial state. (d) the transition states. (e) the final state.

For oxygen diffusion, we use hybrid functional calculation and DFT at the same time to check the accuracy of the DFT method. Here, we use the NEB method to generate 11 intermediate structures to observe the migration. Figure 4.2 shows energy barrier graphs are symmetric, and it consists of the fact that the cubic phase WO3 is symmetric. The energy barrier from the hybrid functional calculation is 0.51 eV, and the energy barrier from the DFT calculation is 0.50 eV, so DFT calculation has similar energy barrier to hybrid DFT. Hybrid

DFT can obtain very accurate total energies but it is too expensive on calculation. Therefore, we use DFT for further monoclinic WO_3 energy barrier calculations.

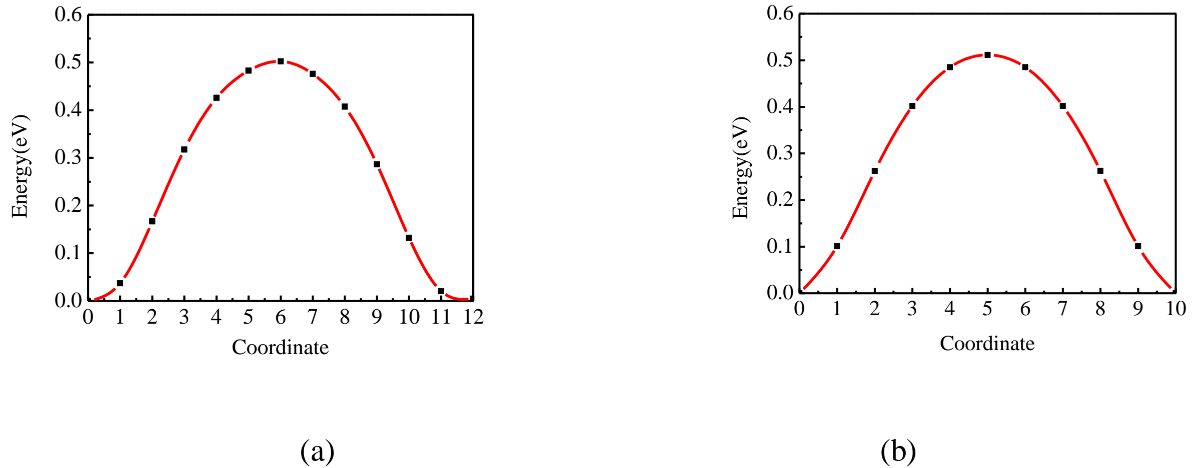

(a) (b)

Figure 4.2 Energy barrier graph. (a) results from DFT calculation. (b) results from Hybrid DFT calculation.

4.2 Monoclinic phase

The rest part of this research is based on the monoclinic phase. The monoclinic bulk is shown in Figure 4.3. Since the monoclinic phase is not symmetric, the single oxygen vacancy will have three non-equivalent positions to migrate, which are parallel to the lattice vectors. Here we label them as positions A, B and C. Parameter of the bulk is in Table 1. We use Hybrid DFT to relax the bulk, then we get a reasonable band gap value and lattice parameters.

Table 1 Lattice parameter and band gap for WO_3 monoclinic phase.

	a (Å)	b(Å)	c (Å)	β (°)	E_g (eV)
Exp.[62]	7.31	7.54	7.69	90.88	2.6-2.8 [63]
This work (HSE)	7.41	7.63	7.79	90.08	2.62
B3LYP[64]	7.44	7.73	7.91	90.20	3.13
PW91[62]	7.50	7.73	7.80	90.30	1.19

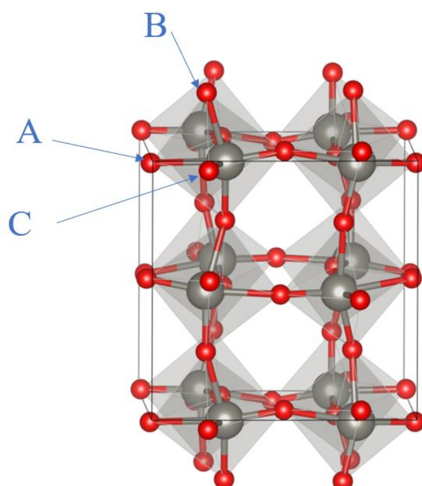

Figure 4.3 Three non-equivalent positions A, B, and C. The red atoms are oxygen and sliver atoms are tungsten. A, B, and C are along the y, z, and x vectors, respectively.

The method of finding the energy barrier is the same as the process described in the cubic phase, while the supercell for monoclinic is 256 atoms. We use the special k-point (1/4, 1/4, 1/4) for these big supercells. We use hybrid DFT to calculate formation energies because formation energies may affect the determination of the most stable charge state and hybrid DFT can obtain more accurate total energies. However, hybrid DFT is less efficient than DFT, and we can still get reliable results from DFT. Therefore, we use DFT for the diffusion barriers for the 256 atoms supercell. We separate the monoclinic phase calculation into two parts: one vacancy and two vacancies in the supercell. We start from one vacancy.

4.2.1 One vacancy

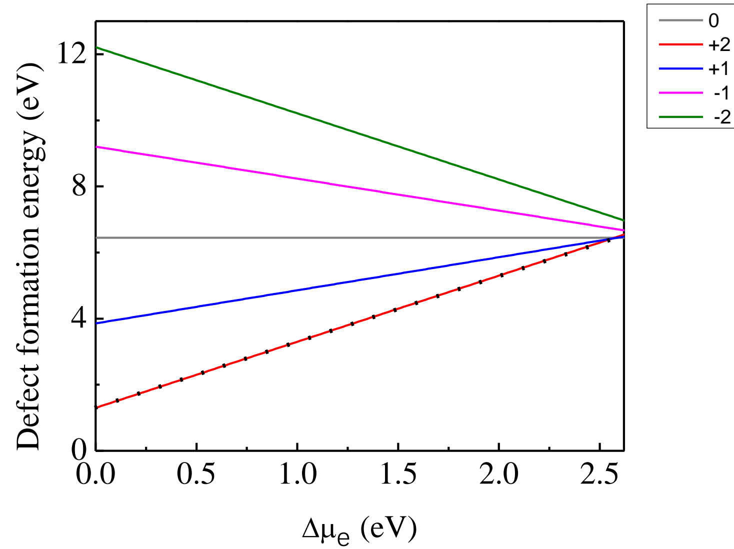

Figure 4.4 Formation energy of the different charge states of the vacancy as a function of the electron chemical potential in monoclinic WO_3.

Figure 4.4 shows the formation energy of one vacancy with possible charge states 2+, 1+, neutral, 1-, 2- in WO3 supercell. The crossing point of the 2+ plot and neutral plot is x=2.576 eV, while the band gap here is 2.62 eV. So neutral is the most stable charge state within the range from 2.576 to 2.62 eV. Hence, the most stable charge state is 2+ and neutral from this graph. Therefore, we will focus on these two charge states for further calculations on one vacancy migration.

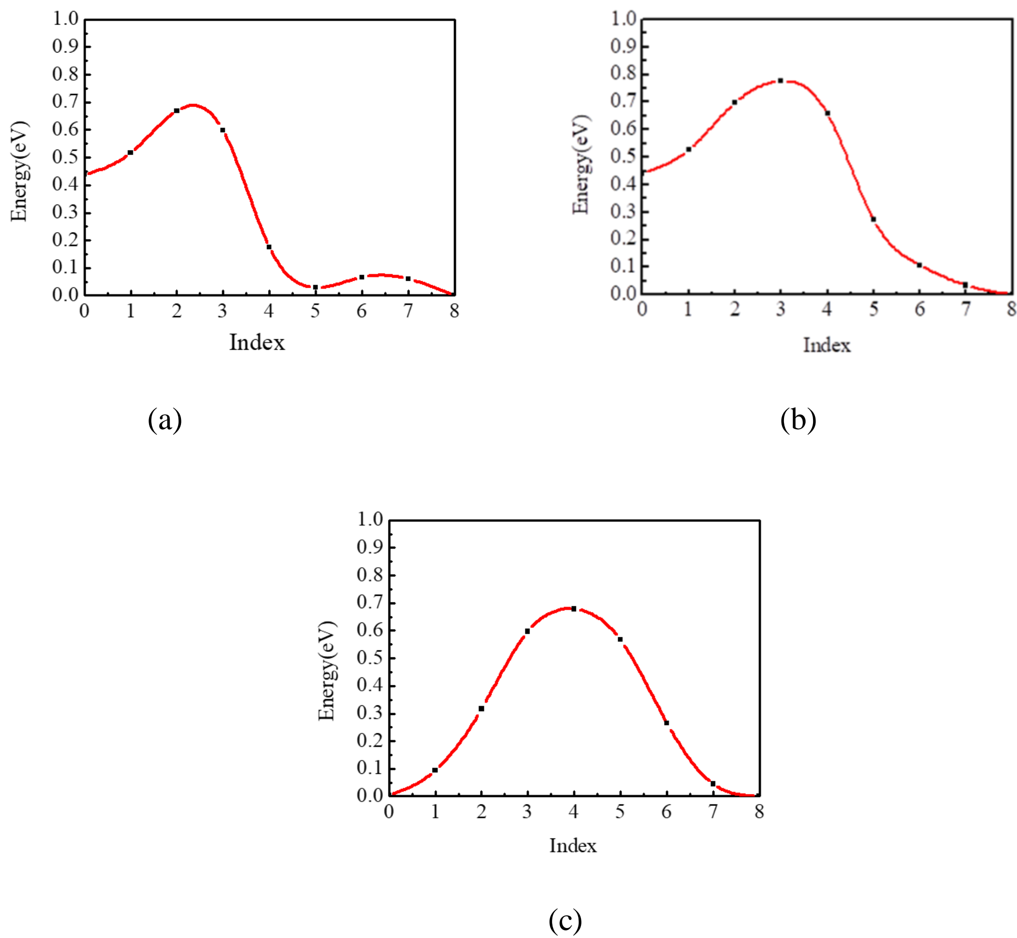

Figure 4.5 Energy barrier of neutral 255-atoms monoclinic WO_3 supercell. (a)vacancy move from A to B. (b)vacancy move from A to C. (c)vacancy move from B to C.

Figure 4.5 shows the energy barriers of the neutral charge state with one vacancy. In Figure 4.5 (a), the initial state is position A in the monoclinic cell and the final state is position B; The energy barrier from B to A is 0.67 eV and from A to B is 0.23 eV. In Figure 4.5(b), the initial state is A; The final state is C; The energy barrier from C to A is 0.77 eV and from A to C is 0.33 eV. In Figure 4.5(c), the initial state is B; The final state is C; The energy barrier from C to B is 0.68 eV and from B to C is 0.67 eV. Figure 4.5 (c) also illustrates that the total energy of vacancy on position B is approximately equal to the total energy of vacancy on position C. After we check the neutral charge state, we move to the 2+ charge state.

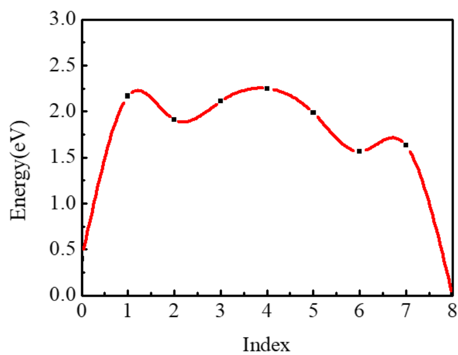

(a)

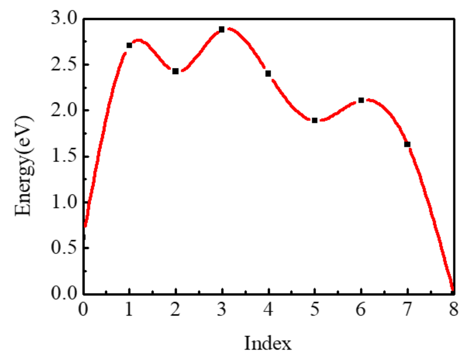

(b)

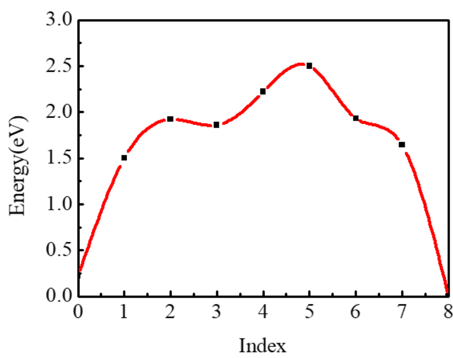

(c)

Figure 4.6 Energy barrier of 2+ charge 255-atoms monoclinic WO_3 supercell. (a)vacancy move from A to B. (b)vacancy move from A to C. (c)vacancy move from B to C.

Figure 4.6 illustrates energy barriers of the 2+ charge state with one vacancy. In Figure 4.6(a), the initial state is A; The final state is B; The energy barrier from B to A is 2.25 eV and from A to B is 1.85 eV. In Figure 4.6(b), The initial state is A; The final state is C; The energy barrier from C to A is 2.88 eV and from A to C is 2.26 eV. In Figure 4.6(c), the initial state is B; The final state is C; The energy barrier from C to B is 2.50 eV and from B to C is 2.28 eV.

4.2.2 Two vacancies

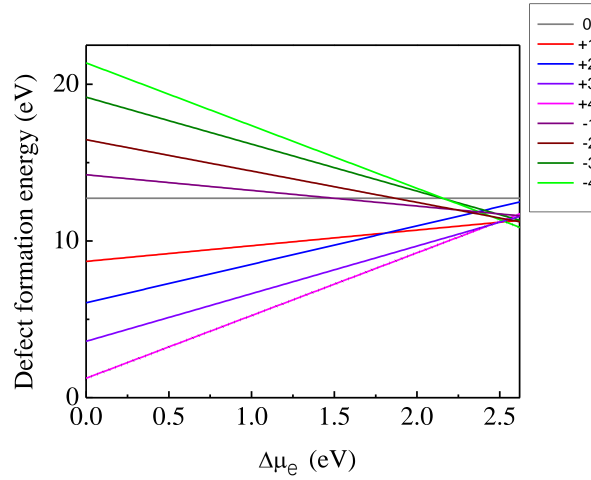

Figure 4.7 Formation energy of all possible charge states of two vacancies as a function of the electron chemical potential in monoclinic WO_3.

Compared to one vacancy, two vacancies situation is more complicated because there are 9 possible charge states. Figure 4.7 is the formation energy of two vacancies. The black dotted line represents the most stable charge state. This graph shows that the most stable charge state is 4+ and 4-. The most stable charge states are 2+ and neutral when there is one vacancy in the structure. The 4+ charge state can be formed by two 2+ divacancies. The 4- is another stable charge state for two vacancies. However, because only neutral and 2+ charge states are stable for a single vacancy, the 4- state of a divacancy can only be formed through the 4+ or neutral di-vacancies capturing electrons. Next, we focus on the interaction between two 2+ or neutral vacancies.

a.

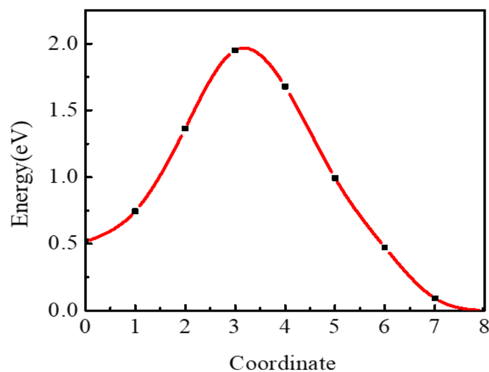

b.

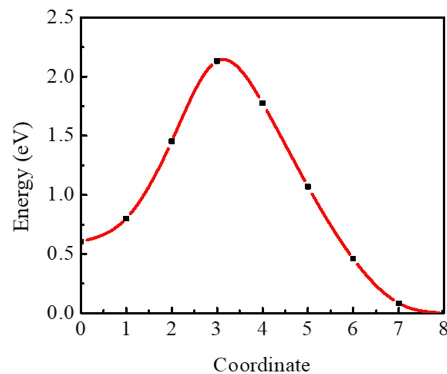

c.

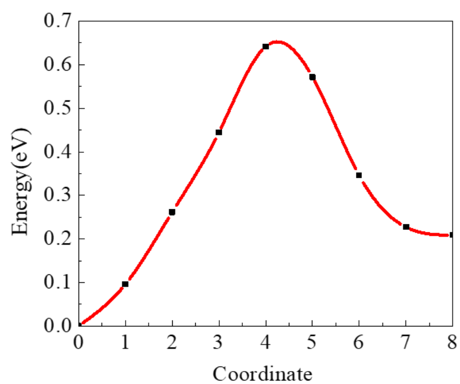

Figure 4.8 The interaction between two vacancies under different charge states.

(a) Vacancies move between A1A2 to CA2 and the charge state is neutral.

(b)Vacancies move between B1B2 to CB2 and the charge state is neutral.

(c) Vacancies move between B1B2 to CB2 and the charge state is +4.

Figure 4.8 shows the interaction between two vacancies under +4 or neutral charge states. Here, we just let one vacancy to move from one position to another and one vacancy not moving at all. For example, in (a), there are two vacancies on position A1 and A2 respectively, we let the vacancy on position A1 move position C, and another one still stays on position A2 without any motion. We can observe the interaction between these two vacancies via comparing it to the condition that just one vacancy in supercell and it moves from A1 to A2. To be more detailed, in

Figure 4.8(a), the energy barrier for vacancies move from positions A1A2 to CA2 is 1.43 eV; from CA2to A1A2 is 1.95 eV. In Figure 4.8(b), the energy barrier from B1B2 to CB2 is 1.53 eV; from CB2 to B1B2 is 2.13 eV. In Figure 4.8(c), the energy barrier from B1B2 to CB2 is 0.64 eV, from CB2 to B1B2 is 0.43 eV.

To describe the motion clearly, we introduce the definition of diffusion limit and reaction limit here. In a chemical reaction A+B→C, it can always be separated into two steps. Step 1, (A+B→AB), material A and B diffuse respectively, and contact with each other. Step 2, (AB→C), the A and B react to form final product C. We can distinguish these two terms by comparing the time of diffusion and reaction. If the diffusion time is much longer than reaction time, in other words, the reactants quickly react right after they finish long-time migration, then the whole procedure is diffusion controlled, and limitation depends on the diffusion limit [65]. On the contrary, if the diffusion process takes a shorter time than the reaction process, then it is reaction controlled, and the reaction limit [66] decides the highest energy the system needs. In this kind of condition, we can add catalysts to cut down reaction time.

If we compare Figure 4.8 graphs with the one vacancy migration energy barrier graphs, we know that (1) it is easier for two vacancies to migrate in 4+ charge state (less than 1 eV) than one vacancy migrates in 2+ charge state (more than 2 eV). It has a large diffusion barrier and small reaction barrier, so it is diffusion limited. (2) Two 2+ vacancies significantly reduce the energy barrier value, so they have a high possibility of getting close to each other. (3) It is harder for two vacancies (more than 1 eV) than one vacancy (less than 1 eV) to migrate in neutral charge state. It has a small diffusion barrier and large reaction barrier, so it is reaction limited. (4) Two neutral vacancies increase the value of energy barriers; it means they are hard to

combine. (5) Since the energy barriers for divacancies have a larger difference than the energy barrier of one vacancy, we cannot use one vacancy as a model when the concentration of vacancies is high.

In Figure 4.8, the total energy of structure with two vacancies on positions A1 and A2 is higher than the structure with two vacancies on positions C and A2. In other words, for the diffusion from A1A2 to CA2, the initial energy is lower than the final energy which causes instability of the final product. The reverse reaction occurs, so there will not be a lot of final products.

Chapter 5

Conclusions and Future Work

In summary, we looked at the diffusivity of the vacancies in WO_3. We determined that the most stable charge state for one vacancy in monoclinic WO_3 is 2+ and neutral. The most stable charge state for two vacancies in monoclinic WO_3 is 4+ and 4-. The 4+ state is formed by 2+ charge divacancies. The 4- state of a divacancy can only be formed through the 4+ or neutral divacancies capturing electrons. The formation of divacancy in the neutral charge state is reaction limited, and the formation of deviancies in 4+ charge state is diffusion limited. It is easy for two 2+ charge vacancies to attract each other, while it is difficult for neutral divacancies to combine. we cannot just use one vacancy case to make models when the concentration of vacancies is high.

Base on the results, we can model how the distribution of vacancies change in WO_x as a function of time. After we know the distribution of vacancies, it is possible to predict the width of the Schottky barrier. Since the Schottky barrier is related to the value of current, so we can model current changes and resistance changes. Finally, we can get an accurate model for the switching of WO_x memristors.

References

[1] R. Naous, "Von-Neumann and Beyond : Memristor Architectures," 2017.

[2] S. N. Abdulkader, A. Atia, and M. S. M. Mostafa, "Brain computer interfacing: Applications and challenges," *Egypt. Informatics J.*, vol. 16, no. 2, pp. 213–230, 2015, doi: 10.1016/j.eij.2015.06.002.

[3] D. Ma, G. Wang, C. Han, Y. Shen, and Y. Liang, "A Memristive Neural Network Model with Associative Memory for Modeling Affections," *IEEE Access*, 2018, doi: 10.1109/ACCESS.2018.2875433.

[4] C. Frenkel, M. Lefebvre, J. D. Legat, and D. Bol, "A 0.086-mm2 12.7-pJ/SOP 64k-Synapse 256-Neuron Online-Learning Digital Spiking Neuromorphic Processor in 28-nm CMOS," *IEEE Trans. Biomed. Circuits Syst.*, vol. 13, no. 1, pp. 145–158, 2019, doi: 10.1109/TBCAS.2018.2880425.

[5] D. B. Strukov, G. S. Snider, D. R. Stewart, and R. S. Williams, "The missing memristor found," *Nature*, vol. 453, no. 7191, pp. 80–83, May 2008, doi: 10.1038/nature06932.

[6] "The memristor revisited," *Nat. Electron.*, vol. 1, no. 5, p. 261, 2018, doi: 10.1038/s41928-018-0083-3.

[7] M. Mahvash and A. C. Parker, "A memristor SPICE model for designing memristor circuits," in *Midwest Symposium on Circuits and Systems*, 2010, doi: 10.1109/MWSCAS.2010.5548803.

[8] M. Di Ventra, Y. V. Pershin, and L. O. Chua, "Circuit elements with memory: Memristors, memcapacitors, and meminductors," *Proc. IEEE*, 2009, doi: 10.1109/JPROC.2009.2021077.

[9] L. O. Chua, "Memristor—The Missing Circuit Element," *IEEE Trans. Circuit Theory*, vol. 18, no. 5, pp. 507–519, 1971, doi: 10.1109/TCT.1971.1083337.

[10] L. Wang, C. H. Yang, J. Wen, S. Gai, and Y. X. Peng, "Overview of emerging memristor families from resistive memristor to spintronic memristor," *J. Mater. Sci. Mater.*

Electron., vol. 26, no. 7, pp. 4618–4628, 2015, doi: 10.1007/s10854-015-2848-z.

[11] Y. Zuo *et al.*, “Effect of the Pressure Exerted by Probe Station Tips in the Electrical Characteristics of Memristors,” *Adv. Electron. Mater.*, 2020, doi: 10.1002/aelm.201901226.

[12] A. Sawa, “Resistive switching in transition metal oxides,” *Mater. Today*, vol. 11, no. 6, pp. 28–36, 2008, doi: 10.1016/S1369-7021(08)70119-6.

[13] K. M. Kim, B. J. Choi, and C. S. Hwang, “Localized switching mechanism in resistive switching of atomic-layer-deposited Ti O2 thin films,” *Appl. Phys. Lett.*, vol. 90, no. 24, 2007, doi: 10.1063/1.2748312.

[14] T. Chang, S. H. Jo, K. H. Kim, P. Sheridan, S. Gaba, and W. Lu, “Synaptic behaviors and modeling of a metal oxide memristive device,” *Appl. Phys. A Mater. Sci. Process.*, vol. 102, no. 4, pp. 857–863, 2011, doi: 10.1007/s00339-011-6296-1.

[15] W. Y. Chang, C. A. Lin, J. H. He, and T. B. Wu, “Resistive switching behaviors of ZnO nanorod layers,” *Appl. Phys. Lett.*, vol. 96, no. 24, pp. 2–5, 2010, doi: 10.1063/1.3453450.

[16] X. Shen, Y. S. Puzyrev, and S. T. Pantelides, “Vacancy breathing by grain boundaries - A mechanism of memristive switching in polycrystalline oxides,” *MRS Commun.*, 2013, doi: 10.1557/mrc.2013.32.

[17] S. Kvatinsky, E. G. Friedman, A. Kolodny, and U. C. Weiser, “The desired memristor for circuit designers,” *IEEE Circuits Syst. Mag.*, 2013, doi: 10.1109/MCAS.2013.2256257.

[18] A. Beck, J. G. Bednorz, C. Gerber, C. Rossel, and D. Widmer, “Reproducible switching effect in thin oxide films for memory applications,” *Appl. Phys. Lett.*, 2000, doi: 10.1063/1.126902.

[19] G. H. Kim *et al.*, “32 × 32 crossbar array resistive memory composed of a stacked schottky diode and unipolar resistive memory,” *Adv. Funct. Mater.*, 2013, doi: 10.1002/adfm.201202170.

[20] L. Chua, “Resistance switching memories are memristors,” *Appl. Phys. A Mater. Sci. Process.*, 2011, doi: 10.1007/s00339-011-6264-9.

[21] S. E. Savel'Ev, A. S. Alexandrov, A. M. Bratkovsky, and R. Stanley Williams, "Molecular dynamics simulations of oxide memory resistors (memristors)," *Nanotechnology*, 2011, doi: 10.1088/0957-4484/22/25/254011.

[22] D. Ielmini, C. Cagli, and F. Nardi, "Resistance transition in metal oxides induced by electronic threshold switching," *Appl. Phys. Lett.*, vol. 94, no. 6, pp. 1–4, 2009, doi: 10.1063/1.3081401.

[23] J. Guo *et al.*, "Reconfigurable resistive switching devices based on individual tungsten trioxide nanowires," *AIP Adv.*, 2013, doi: 10.1063/1.4804067.

[24] W. Xue, S. Gao, J. Shang, X. Yi, G. Liu, and R. W. Li, "Recent Advances of Quantum Conductance in Memristors," *Advanced Electronic Materials*. 2019, doi: 10.1002/aelm.201800854.

[25] Z. Zheng, "Synthesis and Modifications of Metal Oxide Nanostructures and Their Applications," *Queensl. Univ. Technol.*, 2009.

[26] W. Sun *et al.*, "Understanding memristive switching via in situ characterization and device modeling," *Nat. Commun.*, vol. 10, no. 1, pp. 1–13, 2019, doi: 10.1038/s41467-019-11411-6.

[27] S. Porro and C. Ricciardi, "Memristive behaviour in inkjet printed graphene oxide thin layers," *RSC Adv.*, 2015, doi: 10.1039/c5ra11058k.

[28] K. Noda, Y. Wada, and T. Toyabe, "Schottky contact," *Phys. Chem. Chem. Phys.*, 2015, doi: 10.1039/C4CP01792G.

[29] Y. Shen, A. R. Hosseini, M. H. Wong, and G. G. Malliaras, "How to make ohmic contacts to organic semiconductors," *ChemPhysChem*. 2004, doi: 10.1002/cphc.200300942.

[30] L. M. Porter and R. F. Davis, "A critical review of ohmic and rectifying contacts for silicon carbide," *Materials Science and Engineering B*. 1995, doi: 10.1016/0921-5107(95)01276-1.

[31] A. V. Polotai *et al.*, "Effect of Cr additions on the electrical properties of Ni-BaTiO3 ultra-thin multilayer capacitors," *J. Electroceramics*, 2009, doi: 10.1007/s10832-008-

9496-0.

[32] D. S. Jeong, H. Schroeder, and R. Waser, “Mechanism for bipolar switching in a Pt/ TiO2 /Pt resistive switching cell,” *Phys. Rev. B - Condens. Matter Mater. Phys.*, vol. 79, no. 19, pp. 1–10, 2009, doi: 10.1103/PhysRevB.79.195317.

[33] K. Ando, S. Fujita, M. Hayashikoshi, and Y. Fujimori, “Non-volatile memories,” in *Normally-Off Computing*, 2017.

[34] H. WATANABE, “MOS Transistor,” *J. Inst. Electr. Eng. Japan*, 2008, doi: 10.1541/ieejjournal.128.154.

[35] J. S. Meena, S. M. Sze, U. Chand, and T. Y. Tseng, “Overview of emerging nonvolatile memory technologies,” *Nanoscale Res. Lett.*, 2014, doi: 10.1186/1556-276X-9-526.

[36] I. Ferain, C. A. Colinge, and J. P. Colinge, “Multigate transistors as the future of classical metal-oxide-semiconductor field-effect transistors,” *Nature*. 2011, doi: 10.1038/nature10676.

[37] S. W. Lee, S. J. Park, E. E. B. Campbell, and Y. W. Park, “A fast and low-power microelectromechanical system-based non-volatile memory device,” *Nat. Commun.*, 2011, doi: 10.1038/ncomms1227.

[38] A. Kawaguchi, S. Nishioka, and H. Motoda, “A flash-memory based file system,” in *USENIX 1995 Technical Conference Proceedings*, 1995.

[39] A. Sawa, “Resistive switching in Rapid advances in information technology rely on high-speed and,” *Mater. Today*, 2008, doi: 10.1016/S1369-7021(08)70119-6.

[40] A. Buscarino, L. Fortuna, M. Frasca, and L. V. Gambuzza, “A gallery of chaotic oscillators based on hp memristor,” *Int. J. Bifurc. Chaos*, 2013, doi: 10.1142/S0218127413300152.

[41] M. J. Berridge, “Neuronal Signalling,” *Cell Signal. Biol.*, 2014, doi: 10.1042/csb0001010.

[42] E. E. Benarroch, “Neuron-astrocyte interactions: Partnership for normal function and disease in the central nervous system,” in *Mayo Clinic Proceedings*, 2005, doi: 10.4065/80.10.1326.

[43] C. Hammond, J. M. Goaillard, D. Debanne, and J. L. Gaiarsa, “Synaptic plasticity,” in *Cellular and Molecular Neurophysiology: Fourth Edition*, 2015.

[44] T. Chang, “Tungsten Oxide Memristive Devices for Neuromorphic Applications,” *Thesis*, 2012.

[45] S. Royer and D. Paré, “Conservation of total synaptic weight through balanced synaptic depression and potentiation,” *Nature*, 2003, doi: 10.1038/nature01530.

[46] N. Ilyas, D. Li, C. Li, X. Jiang, Y. Jiang, and W. Li, “Analog Switching and Artificial Synaptic Behavior of Ag/SiOx:Ag/TiOx/p++-Si Memristor Device,” *Nanoscale Res. Lett.*, 2020, doi: 10.1186/s11671-020-3249-7.

[47] C. Wang, W. He, Y. Tong, and R. Zhao, “Investigation and Manipulation of Different Analog Behaviors of Memristor as Electronic Synapse for Neuromorphic Applications,” *Sci. Rep.*, 2016, doi: 10.1038/srep22970.

[48] P. S. Maheshwar, C. Yang, H. Kim, and L. Chua, “A voltage mode memristor bridge synaptic circuit with memristor emulators,” *Sensors*, 2012, doi: 10.3390/s120303587.

[49] S. G. Dahl, R. C. Ivans, and K. D. Cantley, “Learning behavior of memristor-based neuromorphic circuits in the presence of radiation,” in *ACM International Conference Proceeding Series*, 2019, doi: 10.1145/3354265.3354272.

[50] A. H. Edwards, H. J. Barnaby, K. A. Campbell, M. N. Kozicki, W. Liu, and M. J. Marinella, “Reconfigurable memristive device technologies,” *Proc. IEEE*, 2015, doi: 10.1109/JPROC.2015.2441752.

[51] S. H. Lee, “Hybrid Memristor-CMOS Computer for Artificial Intelligence : from Devices to Systems by,” 2020.

[52] S. Shriwastava and C. C. Tripathi, “Metal–Insulator–Metal Diodes: A Potential High Frequency Rectifier for Rectenna Application,” *Journal of Electronic Materials*. 2019, doi: 10.1007/s11664-018-06887-9.

[53] F. Corsetti and A. A. Mostofi, “System-size convergence of point defect properties: The case of the silicon vacancy,” *Phys. Rev. B - Condens. Matter Mater. Phys.*, 2011, doi:

10.1103/PhysRevB.84.035209.

[54] D. W. Ball, "The Born-Oppenheimer Approximation," in *Field Guide to Spectroscopy*, 2009.

[55] K. Capelle, "A bird's-eye view of density-functional theory," in *Brazilian Journal of Physics*, 2006, doi: 10.1590/s0103-97332006000700035.

[56] R. M. M. Uiuc, "Density Functional Theory The Basis of Most Modern Calculations," *Structure*, 2005.

[57] M. Levy, J. P. Perdew, and V. Sahni, "Exact differential equation for the density and ionization energy of a many-particle system," *Phys. Rev. A*, 1984, doi: 10.1103/PhysRevA.30.2745.

[58] X. Shen, Y. S. Puzyrev, D. M. Fleetwood, R. D. Schrimpf, and S. T. Pantelides, "Quantum mechanical modeling of radiation-induced defect dynamics in electronic devices," *IEEE Trans. Nucl. Sci.*, vol. 62, no. 5, pp. 2169–2180, 2015, doi: 10.1109/TNS.2015.2470665.

[59] L. Piela, "Chasing Correlation Dragon: Density Functional Theory (DFT)," in *Ideas of Quantum Chemistry*, 2014.

[60] W. Kohn and L. J. Sham, "Self-consistent equations including exchange and correlation effects," *Phys. Rev.*, 1965, doi: 10.1103/PhysRev.140.A1133.

[61] W. Wang, A. Janotti, and C. G. Van De Walle, "Role of oxygen vacancies in crystalline WO3," *J. Mater. Chem. C*, vol. 4, no. 27, pp. 6641–6648, 2016, doi: 10.1039/c6tc01643j.

[62] F. Di Quarto, A. Di Paola, and C. Sunseri, "Semiconducting properties of anodic WO3 amorphous films," *Electrochim. Acta*, 1981, doi: 10.1016/0013-4686(81)85095-5.

[63] P. P. González-Borrero *et al.*, "Optical band-gap determination of nanostructured WO3 film," *Appl. Phys. Lett.*, 2010, doi: 10.1063/1.3313945.

[64] F. Wang, C. Di Valentin, and G. Pacchioni, "Electronic and structural properties of WO3: A systematic hybrid DFT study," *J. Phys. Chem. C*, 2011, doi: 10.1021/jp201057m.

[65] T. A. Witten and L. M. Sander, "Diffusion-limited aggregation, a kinetic critical

phenomenon," *Phys. Rev. Lett.*, 1981, doi: 10.1103/PhysRevLett.47.1400.

[66] D. Fange, O. G. Berg, P. Sjöberg, and J. Elf, "Stochastic reaction-diffusion kinetics in the microscopic limit," *Proc. Natl. Acad. Sci. U. S. A.*, 2010, doi: 10.1073/pnas.1006565107.